

Systematic Modeling of Rotor-Driving Dynamics for Small Unmanned Aerial Vehicles

Limin Wu*, Yijie Ke, Ben M. Chen

*Unmanned Systems Research Group, Department of Electrical and Computer Engineering
Faculty of Engineering, National University of Singapore
4 Engineering Drive 3, 117583 Singapore*

This paper proposes a systematic modeling approach of rotor-driving dynamics for small unmanned aerial vehicles (UAVs) based on system identification and first principle-based methods. Both steady state response analyses and frequency-domain identifications are conducted for the rotor, and Comprehensive Identification from Frequency Responses (CIFER) software is mainly utilized for the frequency-domain analysis. Moreover, a novel semi-empirical model integrating the rotor and the electrical speed controller is presented and validated. The demonstrated results and model are promising in UAV dynamics and control applications.

Keywords: UAV; rotor-driving dynamics; system identification; semi-empirical model.

US

1. Introduction

Serving as a key component for common small unmanned aerial vehicles (UAVs), the rotor-driving dynamics which explains the dynamics of motor, electronic speed controller (ESC) and propeller (MEP) subsystem plays a crucial role in understanding the flight dynamics.

The challenges include the complex propeller aerodynamics and hardware response, which result in the impossibility to obtain a high fidelity model that can be integrated in the flight control. In most works in the literature, the rotor-driving dynamics is usually simplified by utilizing low frequency response information only, such as static thrust and torque. To further improve the flight maneuverability, the dynamics of the MEP subsystem has to be investigated.

System identification is one approach to determine the mathematical model for a system through experimentation. It is a commonly used tool to extract the information of system response around a certain trim condition, such as the steady state and frequency-domain response. There are

prior examples of system identification for rotor subsystem modeling. For example, the work of Ahmad *et al.* in [1] applies identification techniques to estimate a linear time-invariant (LTI) model for a twin rotor MIMO system, and the dynamics of a model-scale helicopter is successfully identified in the work of Mettler *et al.* in [2]. In this work, we design and implement our setup to model the rotor-driving dynamics as LTI Single Input Single Output (SISO) systems. The choice of stimulus signals is a significant factor in the rotor test, and some basis criteria for the design of stimulus signals are introduced in [3] by Ljung. For identification, the work of Chen *et al.* on system identification has demonstrated some commonly used techniques in the time-domain and frequency domain in [4], and these techniques are utilized to model the micro and voice-coil-motor (VCM) actuators in the hard disk drive (HDD) servo systems. However, the limitation of system identification is that, since we are viewing the rotor subsystem as a black box, no insight can be gained explicitly for rotor subsystem which is treated as a black box.

Another modeling approach is the first principle modeling [4], which relies on a deep understanding of underlying physics. There has been much research in the field of modeling of brushless direct current (BLDC) motor. For example, a BLDC motor can be modeled as an electrical

Received 21 April 2017; Revised 2 October 2017; Accepted 3 October 2017; Published 8 June 2018. This paper was recommended for publication in its revised form by editorial board member, Feng Lin.
Email Address: *liminwu89ee@gmail.com

subsystem and a mechanical subsystem for fault detection in [5]. A sensorless control of a BLDC motor is achieved based on voltage and current models in Matsui's work [6]. A more general model using phase variable approach with simplified back EMFs is presented in Pillay's works [7, 8]. However, these methods are still overcomplicated in practice due to many unknown parameters. For the propeller, the blade element theory is the foundation of propeller aerodynamics analysis and it is a relatively simple method to predict the propeller performance in [9, 10].

The modeling of the MEP subsystem is a commonly overlooked challenge in the literature to our best knowledge. Thus, we propose a simplified semi-empirical model integrating BLDC, ESC and propeller models, in order to approximate the rotor-driving dynamics in an effective manner. This method is advantageous in keeping the flexibility of parameters determined through experimental data.

This paper is organized as follows: Section 2 illustrates our methodology for system identification and first principle modeling. Section 3 presents the experiment setup and work flow. Section 4 illustrates the system identification method for rotor response, including both steady state analyses and frequency domain analyses. Responses of thrust force, torque and propeller angular speed are recorded and investigated. Section 5 presents a novel semi-empirical method integrating BLDC motor, propeller and ESC. Conclusions are summarized in Sec. 6.

2. Methodology Overview

2.1. System identification

The work flow of system identification [3] is shown in Fig. 1.

The accuracy of this method depends heavily on the experiment setup and data processing techniques. In our

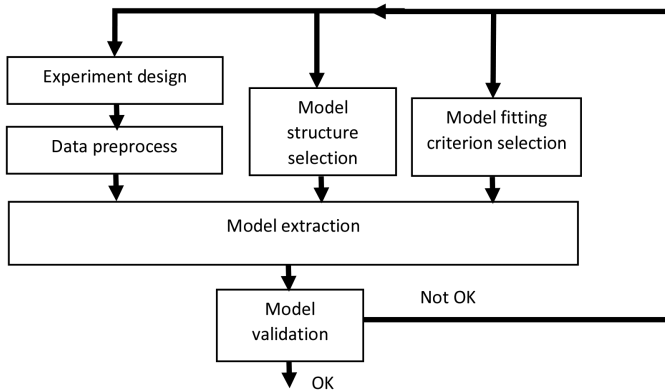


Fig. 1. System identification work flow.

rotor test experiment, the rotor and all sensors are fixed on a rigid metal rack. Since the output bandwidths are unknown, the sampling rate of each sensor is set to its maximum rate. Particular effort is made to synchronize sensor signals. In data preprocess step, techniques like resampling and trimming are used to improve the data quality.

The rest of steps are embedded in CIFER, which is a software developed by U.S. Army and NASA. CIFER is specially designed for rotorcraft applications and has been widely used for fixed-wing, rotary wing and unconventional aircraft applications [11, 12]. Based on the imported time domain data, CIFER identifies frequency response by applying fast Fourier transform and associated windowing techniques. Since we are interested in SISO systems, non-parametric models including Bode plot and parametric models including transfer function model can be fully characterized by frequency-response results. For the choice of model structure, previous research by Cai utilizes the system identification to model the yaw-channel dynamics of a helicopter, and control-system is successfully designed based on the identified linear model [13]. Hence, in our work, the low order transfer function model is used to construct our parametric model. The parameters in the parametric model are determined numerically by fitting the frequency-response data in a least-square sense [11]. For the model validation, the coherence function is used to measure the identification accuracy. It can be obtained from measurement:

$$\gamma_{xy}^2 = \frac{|G_{xy}|^2}{|G_{xx}| |G_{yy}|}, \quad (1)$$

where coherence is γ_{xy} , and G_{xy} , G_{xx} , G_{yy} is the cross spectrum, input and output auto-spectrum, respectively. Coherence can indicate whether the model obtained is well characterized as a linear process in the interested frequency range.

2.2. First principle modeling

In our work, we attempt to apply this technique to model the MEP subsystem of a small UAV. Different from previous system identification approach, the black-box of MEP subsystem is opened and divided into three parts namely BLDC, propeller and ESC.

• BLDC model

For BLDC, Fig. 2 gives a general three-phase structure of BLDC model [8, 14], it can be described as a differential equation:

$$\begin{bmatrix} v_a \\ v_b \\ v_c \end{bmatrix} = R \begin{bmatrix} i_a \\ i_b \\ i_c \end{bmatrix} + \frac{d}{dt} \begin{bmatrix} L & M & M \\ M & L & M \\ M & M & L \end{bmatrix} \begin{bmatrix} i_a \\ i_b \\ i_c \end{bmatrix} + \begin{bmatrix} E_a \\ E_b \\ E_c \end{bmatrix}, \quad (2)$$

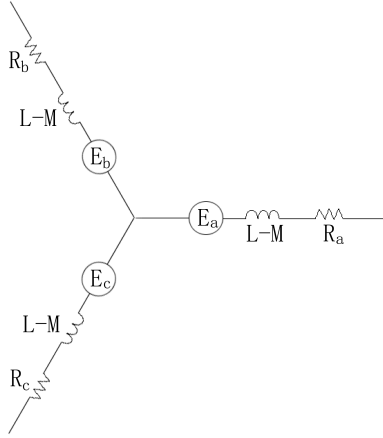


Fig. 2. General BLDC equivalent circuit.

where v_a, v_b, v_c are stator voltages, i_a, i_b, i_c are stator currents, E_a, E_b, E_c are stator back EMFs, R is the resistance with the assumption that $R = R_a = R_b = R_c$, L is the stator self-inductance and M is the mutual inductance between two stators. In order to further simplify this model, we assume that the inductance terms is negligible for low inductance BLDCs. Back EMFs can be estimated by a linear function of the angular speed of rotor [15]. Therefore, Eq. (2) can be simplified to:

$$v = Ri + K_e \omega, \quad (3)$$

where v, R, i are voltage, resistance and current of each stator, ω is angular speed and K_e is the back EMF constant. The motor angular acceleration can be described by:

$$J_r \dot{\omega} = T_m - T_d, \quad (4)$$

where T_m is motor torque and T_d is motor load. In our case, motor load is equivalent to the magnitude of torque produced by propeller.

For a small motor with low inductance, T_m in Eq. (4) can be estimated by a first-order equation [15]; hence Eq. (4) can be rewritten as:

$$J_r \dot{\omega} = -\frac{K_m^2}{R} \omega + \frac{K_m}{R} u - T_d, \quad (5)$$

where J_r is the rotor moment of inertia, K_m is a torque constant, R is resistance in Eq. (3) and v is the voltage input and T_d is the motor load. The magnitude of T_d is equal to the magnitude of T_{total} in the propeller model. Our previous group work [16] further simplified this model into:

$$J_r \dot{\omega} = -K_s - \frac{K_m K_e}{R} \omega - K_r \omega^2 + \frac{K_m}{R} u, \quad (6)$$

where K_s, K_e are also motor electrical parameters.

• Propeller

The Blade element theory used in our work is a simple method to predict the propeller performance, wherein a propeller blade can be discretized to a number of sections. For each section, the local flow schematic in Fig. 3, where θ is the installation pitch angle and α is the local angle of attack (AOA).

The air velocity is decomposed into U_T and U_P which are tangent and perpendicular to the disk plane. Lift and drag forces are produced by the air flow at the blade section. Thrust and torque are obtained by resolving the aerodynamic forces normal and parallel to the disk plane. This theory [17] suggests that the lift and drag forces are:

$$\begin{aligned} L &= \frac{1}{2} \rho U^2 c c_l, \\ D &= \frac{1}{2} \rho U^2 c c_d, \end{aligned} \quad (7)$$

where L is lift, D is drag force, U is the magnitude of air velocity, ρ is air density, c is local chord length and c_l, c_d are lift and drag coefficients. The elemental thrust and torque of a blade element can be written as:

$$\begin{aligned} F &= L \cos \phi - D \sin \phi, \\ \frac{T}{r} &= D \cos \phi + L \sin \phi, \end{aligned} \quad (8)$$

where F is local thrust, T is local torque, r is propeller radius, ϕ is the induced angle from axis flow as shown in Fig. 3. It is clear that c, ρ, c_l, c_d and r are all constants for a specific propeller; and U is proportional to the angular speed. The total thrust and torque of the propeller are obtained by integrating the elemental thrust and torque from Eq. (8) along the entire blade and over one rotor revolution and can be expressed as:

$$\begin{aligned} F_{\text{total}} &= K_f \omega^2, \\ T_{\text{total}} &= K_t \omega^2, \end{aligned} \quad (9)$$

where K_f and K_t are constants for a specific propeller. Therefore, total thrust and torque of a propeller can be estimated simply from angular speed in our propeller model.

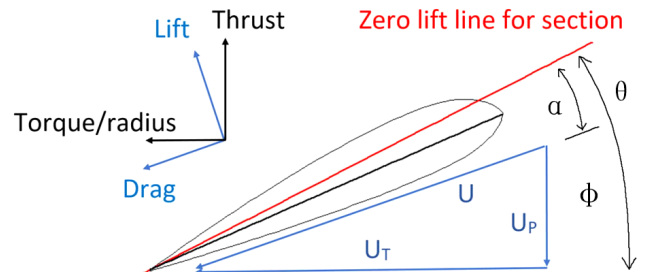


Fig. 3. Schematic of blade section aerodynamics.

Table 1. Switching sequences in the six-step commutation technique.

Step	Phase <i>a</i>	Phase <i>b</i>	Phase <i>c</i>
1	DC+	DC−	NC
2	DC+	NC	DC−
3	NC	DC+	DC−
4	DC−	DC+	NC
5	DC−	NC	DC+
6	NC	DC−	DC+

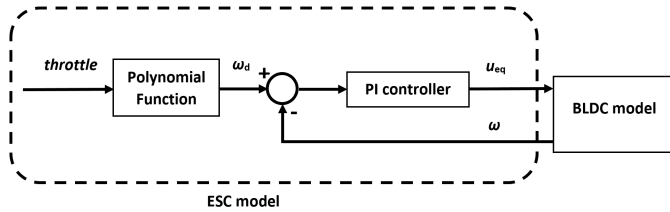


Fig. 4. Schematic of ESC model.

• ESC

Most commercial ESCs are implemented with six-step commutation technique, which controls the switching sequence of the three phases winding as shown in Table 1. The magnetic field generated by the winding keeps changing 60° at each commutation step and a constant rotating direction is achieved [18].

Since most ESCs adopt PI control in their firmware to switch MOSFETs to control BLDC motor as shown in Fig. 4, and previous group research [16] and literature [6] suggested a ESC model:

$$\begin{aligned}
 \omega_d &= K_a \times \text{throttle}^2 + K_b \times \text{throttle} + K_c \\
 e_\omega &= \omega_d - \omega \\
 u_{\text{eq}} &= K_p e_\omega + K_i \int e_\omega dt,
 \end{aligned} \tag{10}$$

where ω_d is a desired angular speed, ω is the actual angular speed, throttle is a normalized throttle between 0 and 1, K_a , K_b and K_c are polynomial coefficients identified in Eq. (11) for relationship between throttle and ω , u_{eq} is the equivalent voltage directly input to BLDC, and K_p , K_i are PI control gains.

With above BLDC, propeller and ESC model elements, we are able to obtain an integrated semi-empirical model to describe the dynamics of the MEP subsystem.

3. Experiment Setup

The experiment aims to capture the dynamics of MEP subsystem under the desired condition. The experiment setup is shown in schematics in Figs. 5 and 6, with

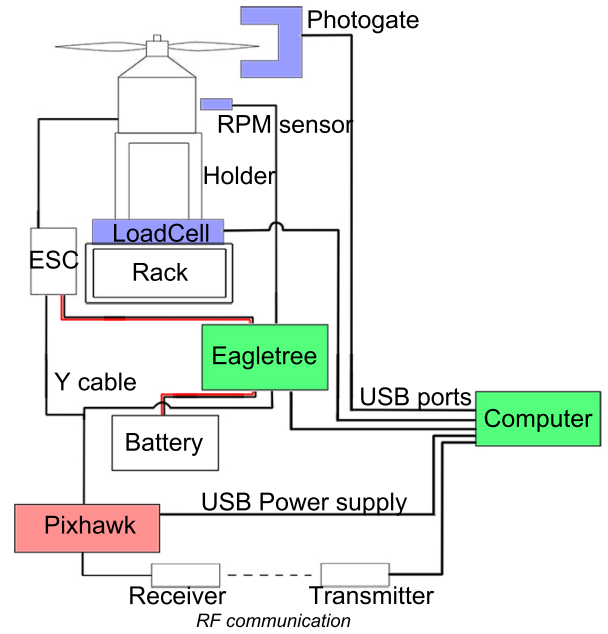


Fig. 5. Schematic of rotor experiment.



Fig. 6. Rotor experiment hardware setup.

Table 2. List of equipments.

Name	Description
APC 11X5.5P Propeller	rotor propeller
Scorpion 3026 motor	brushless DC motor
Scorpion Commander 90A	ESC
4-cells LiPo battery	power supply
optical RPM sensor	angular speed measuring device
Photogate	angular speed measuring device
ATI load cell	6 DOF force and torque logging
Pixhawk	PWM throttle input generator
EagleTree eLogger V4	battery voltage and current recording
rack and holder	supporting platform
computer	sensor data collection

Table 3. List of software programs.

Name	Description
ATI DAQ F/T.NET Demo	Log data from ATI load cell
EagleTree eLogger	Log data from optical RPM sensor
Logger Lite	Log data from Photogate
QGroundControl (QGC)	Send start signal to Pixhawk
Quick Macro	Synchronize software programs

equipments and software programs listed in Tables 2 and 3, respectively.

The input of the MEP subsystem is the normalized throttle from 0.0 to 1.0, and it is generated by Pixhawk at a fixed data rate of 150 Hz. Loadcell can record the force and torque in six degree of freedom with fixed logging rate at 1000 Hz. The Angular speed in RPM can be measured by

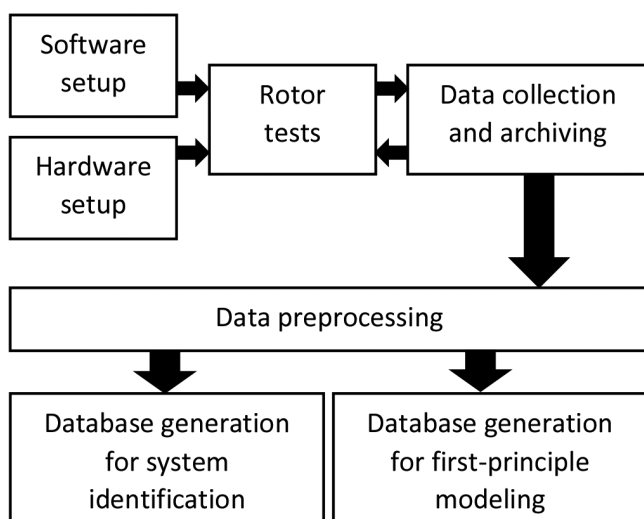


Fig. 7. Experiment work flow.

EagleTree and Photogate devices. EagleTree has a low recording rate of 10 Hz and Photogate can record each revolution of our rotor. The whole setup is powered by a LiPo battery.

The experiment workflow is shown in Fig. 7. The first step includes preparing software programs, charging LiPo batteries and assembling hardware. Then, rotor tests are repeated until all stimulus signals are tested and corresponding data are properly collected. Data preprocessing is accomplished under Matlab environment, this procedure includes synchronizing data, resampling data and trimming data. Finally, database are generated for system identification and first principle modeling.

4. Steady State and Frequency Analysis

Both steady state analysis and frequency-domain identification methods are utilized for rotor dynamics based on our experiment setup. The steady state response can help identify step-response features for interested states, while frequency response can extract richer dynamics information around a trim condition. In this section, main results of these two methods will be presented, and we are mainly concerned with the propeller thrust, torque and angular speed.

4.1. Steady state analysis

4.1.1. Stimulus signal

The stimulus signal for steady state analysis is shown in lower part of Fig. 8, including 10 step inputs increased from 0.1 to 1.0. The total duration is 50 sec.

4.1.2. Angular speed channel

With the steady-state angular speed collected in Table 4 and Fig. 8, an obvious quadratic relationship can be revealed between steady angular speed and throttle input as shown below:

$$\omega = -1080u^2 + 1952u + 42 \quad (0 \leq u \leq 1), \quad (11)$$

where ω is angular speed in rad/s and u is normalized throttle.

4.2. Frequency domain analysis

4.2.1. Stimulus signal

The stimulus signal for the frequency domain analysis is selected to be a sinusoidal wave sweeping from 0.05 Hz to 20 Hz at an equilibrium point with throttle input that equals 0.6. In order to eliminate the effect from battery voltage

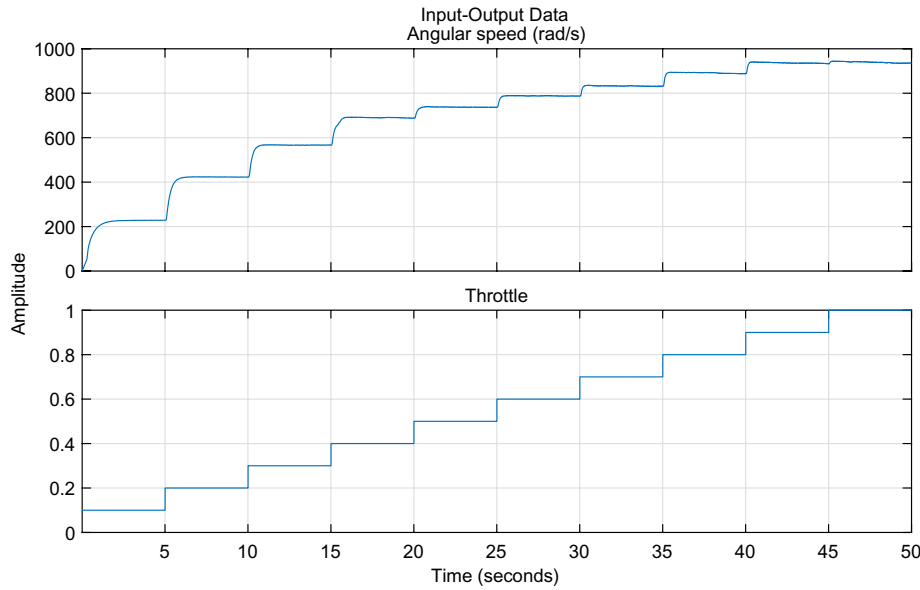


Fig. 8. Plot of measured angular speed with corresponding throttle in step signal test.

Table 4. Data of steady state angular speed at trim throttle conditions.

Throttle	Steady-state Angular speed (rad/sec)
0.10	228.18
0.20	423.17
0.30	566.85
0.40	689.58
0.50	737.54
0.60	788.02
0.70	832.84
0.80	892.74
0.90	937.35
1.00	941.54

drop, the duration of each experiment is limited within 60 seconds, and the chirp signal test is divided into three experiments below. All three chirp signals are plotted in Fig. 9.

- Experiment 1: Chirp signal swept from 0.05 Hz to 0.5 Hz, test duration 50 sec includes 10 sec warm-up.
- Experiment 2: Chirp signal swept from 0.5 Hz to 5 Hz, test duration 50 sec includes 10 sec warm-up.
- Experiment 3: Chirp signal swept from 5 Hz to 20 Hz, test duration 50 sec includes 10 sec warm-up.

4.2.2. Thrust channel

The responses of thrust channel in Experiments 1–3 are shown in Figs. 10–12. The bode plot in frequency domain is

obtained in Fig. 13 in CIFER. Note that the first 10 sec warm-up section and mean value are removed by CIFER during data preprocessing because the response near equilibrium is our interest.

From Fig. 13, the subsystem in thrust channel has a decreasing gain with frequency. The plot of coherence in Fig. 13 indicates the accuracy of frequency estimation. For rotorcraft, a recommended threshold coherence value is 0.6 according to [19]. Therefore, Fig. 13 implies that the estimation is credible within the range of frequency up to 30 rad/s. Phase plot suggests that system have a -135° phase at 30 rad/s. Hence, the system can be approximated by a second order system within confidence domain. Then parameter identification is applied and identified result is

$$\frac{8859}{(s + 9.35)(s + 61.52)}, \quad (12)$$

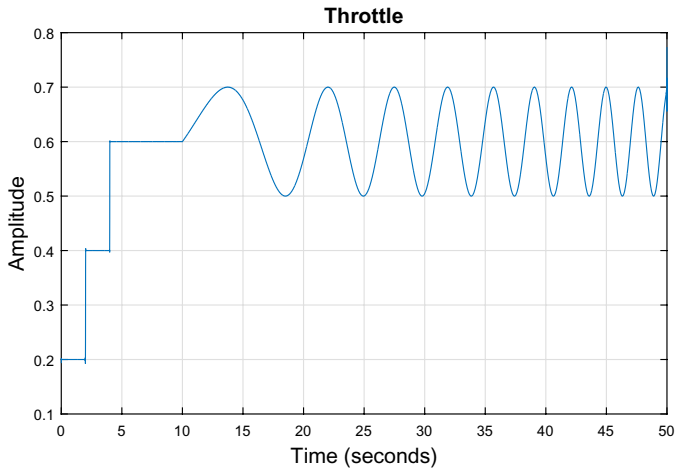
of which DC gain is 23.75 dB, and the bandwidth is 9.12 rad/s.

4.2.3. Torque channel and angular speed channel

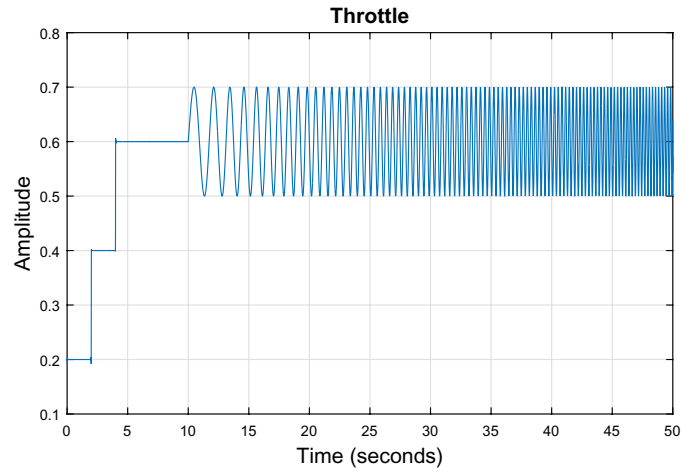
Similar to the thrust channel, the analysis is conducted for torque channel and angular speed channel. The frequency response of torque channel is shown in Fig. 14 and the identified transfer function is

$$23.96 \frac{(s + 6.02)}{(s + 16.94)(s + 33.97)}, \quad (13)$$

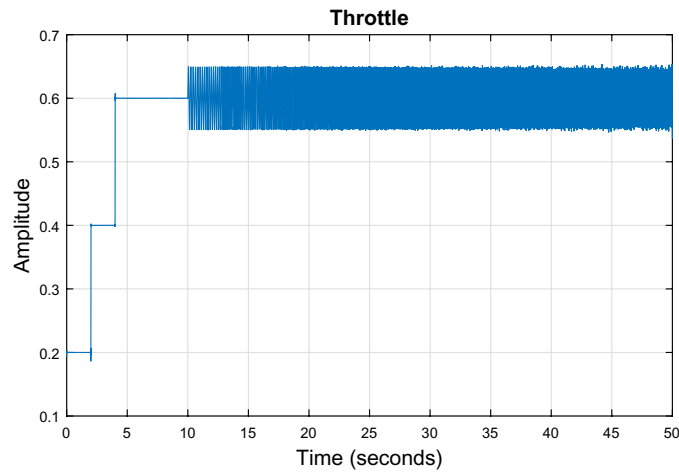
of which DC gain is -12.04 dB, and bandwidth is 129.52 rad/s. The difference between torque channel and thrust



(a) Experiment 1



(b) Experiment 2



(c) Experiment 3

Fig. 9. Chirp stimulus signal.

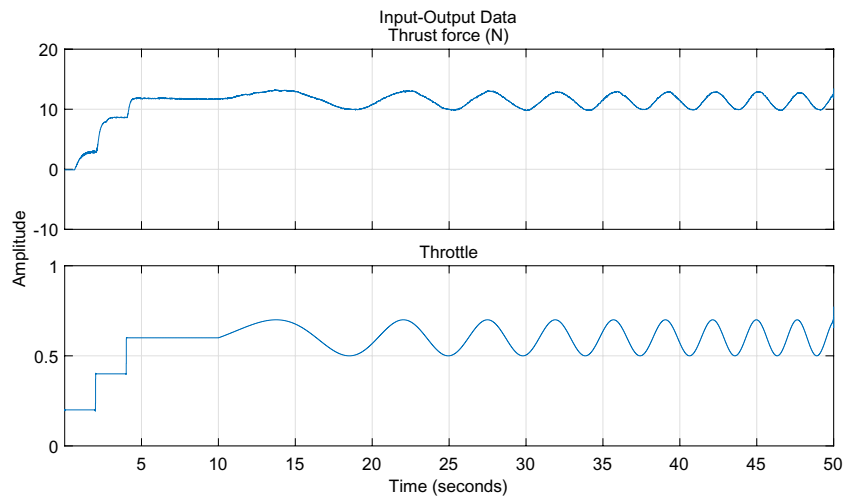


Fig. 10. Thrust channel, time domain data of experiment 1.

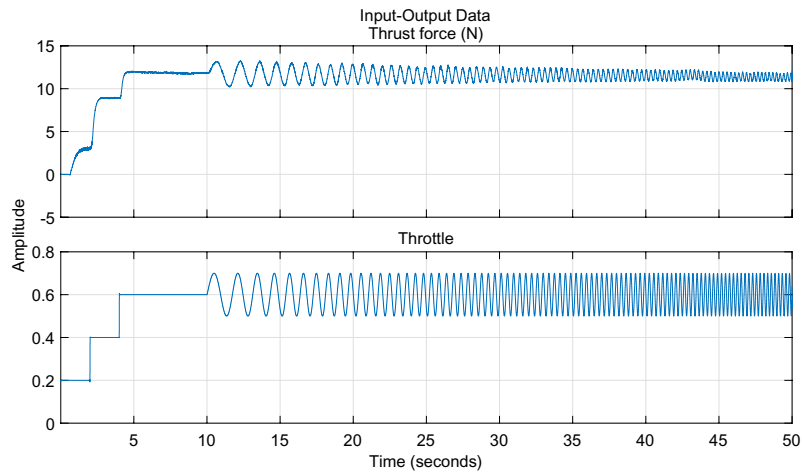


Fig. 11. Thrust channel, time domain data of experiment 2.

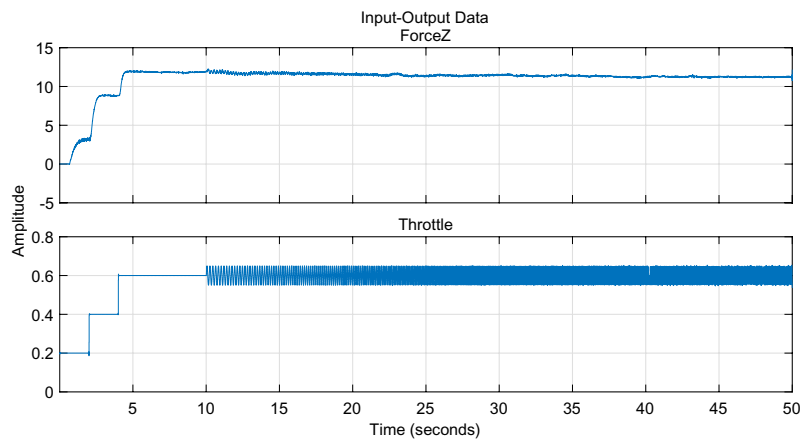


Fig. 12. Thrust channel, time domain data of experiment 3.

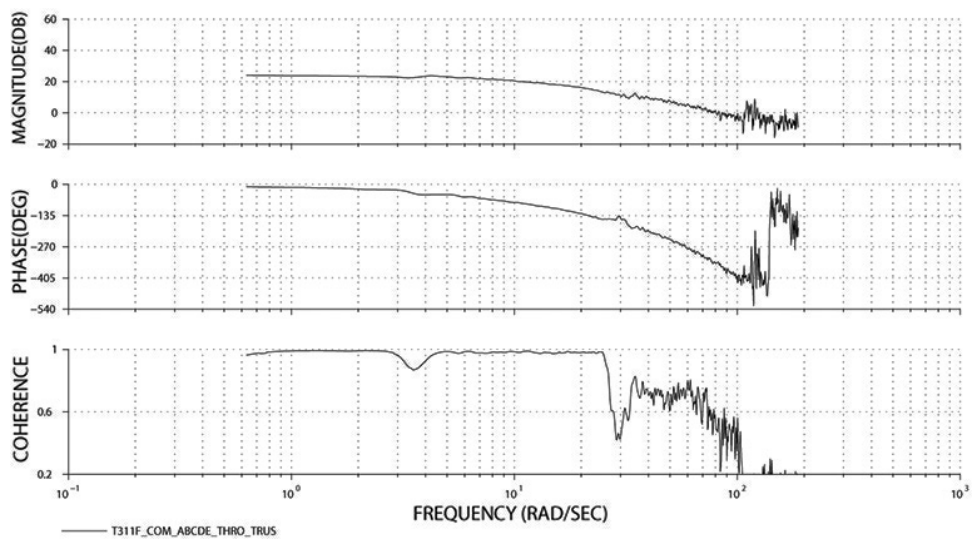


Fig. 13. Thrust channel, Bode plot estimated by CIFER.

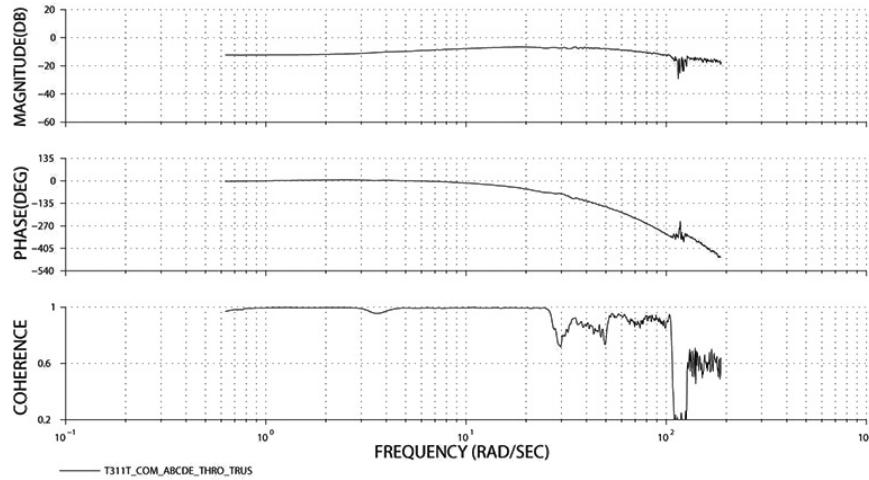


Fig. 14. Torque channel, Bode plot estimated by CIFER.

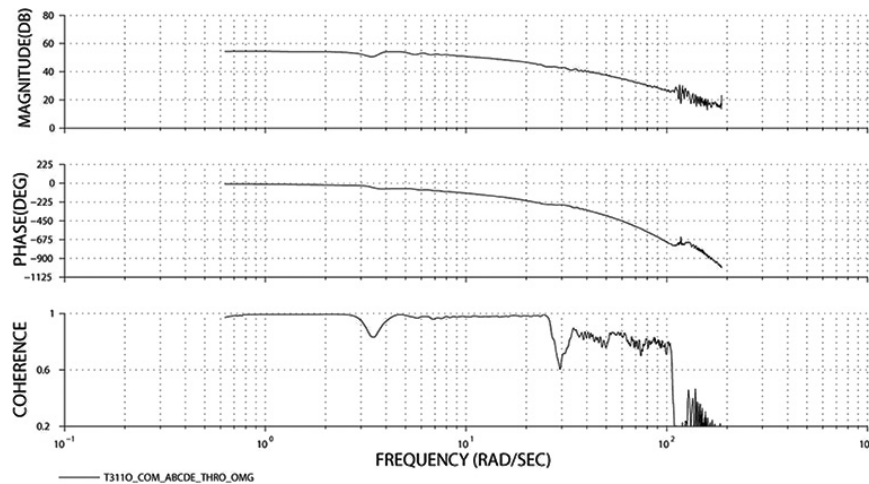


Fig. 15. Angular speed channel, bode plot estimated by CIFER.

channel can be caused by the high frequency lateral resonance mode in the testbed. In contrast, the vertical direction of the testbed is well constrained by the ground and gravity, hence little resonance is excited.

The frequency response of the angular speed channel is shown in Fig. 15 and identified transfer function is

$$\frac{225961}{(s + 9.39)(s + 45.34)}, \quad (14)$$

of which DC gain is 54.48 dB, and bandwidth is 9.01 rad/s.

5. Semi-Empirical Modeling

In previous section, the MEP subsystem is considered as a black-box. The result of identification cannot describe what is happening inside the black-box. In this section, the model

of MEP subsystem will be divided into three parts named ESC model, BLDC model and propeller model. Figure 16 shows the block diagram of the the semi-empirical MEP model.

5.1. Propeller model

The propeller model describes the response from the angular speed to the thrust and the torque. Based on Eq. (7),

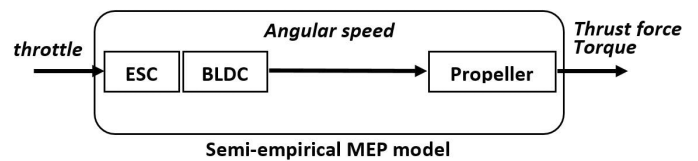


Fig. 16. Components of the semi-empirical MEP model.

constant bias terms are added below:

$$\begin{aligned} F &= K_f \omega^2 + F_{\text{offset}} \\ T &= K_t \omega^2 + T_{\text{offset}}, \end{aligned} \quad (15)$$

where F is thrust force, T is torque, and ω is angular speed in rad/s. K_f , K_t , F_{offset} and T_{offset} are unknown coefficients to be identified. This model is estimated via polynomial fitting based on experimental data, and the result is

$$\begin{aligned} K_f &= 1.814657 \times 10^{-5} \\ F_{\text{offset}} &= -4.376713 \times 10^{-1} \\ K_t &= 2.798821 \times 10^{-7} \\ T_{\text{offset}} &= -5.700314 \times 10^{-3}. \end{aligned} \quad (16)$$

5.2. ESC model and BLDC model

As only the throttle input and the angular speed ω are measurable, a nonlinear model for ESC and BLDC subsystem is derived as below from Eq. (6) and Eq. (10) with an augmented state x_a :

$$\begin{aligned} \dot{\omega} &= -\frac{K_s}{J_r} - \frac{K_m K_e}{R J_r} \omega - \frac{K_r}{J_r} \omega^2 + \frac{K_m K_i}{R J_r} x_a + \frac{K_p K_m}{R J_r} \omega_d \\ \dot{x}_a &= -\omega + \omega_d, \end{aligned} \quad (17)$$

where x_a is an augmented state accounting for the control error, ω_d is the desired angular speed and it can be estimated with the steady angular speed in Eq. (11), K_s , K_m , K_e , K_p , K_r , R and J_r are positive parameters to be identified. This function explains the relation between input throttle and ω_d has been estimated in Eq. (11).

5.3. Estimation of parameter range

- **Effective motor resistance**
 R is the effective Motor Resistance. It can be found in motor datasheet.
- **Rotor inertia**
 J_r is the moment of inertia of rotor. This parameter can be estimated by considering them as a thin rod rotating above its middle point.
- **Equivalent drag coefficient**
 $K_r \omega^2$ represents the reaction torque from the propeller. Therefore, K_r is equivalent to the drag coefficient K_f obtained in Sec. 5.1.
- **Motor torque constant**
The motor torque constant K_m can be calculated by applying the following formula:

$$K_m = \frac{60}{2\pi K_v}, \quad (18)$$

where K_v is the motor velocity constant given in motor data sheet.

- **Back EMF constant**
The Back EMF constant K_e . According to [20], in the three phase BLDC motors the relationship is approximately equal to

$$K_e = \sqrt{\frac{3}{2}} K_m. \quad (19)$$

- **Static friction torque constant**
 K_s is the static friction torque constant and it can be measured by a torque meter. Since this constant usually has much less effect to torque when compared with back EMF and reaction torque of propeller, it is assumed that the friction term have 2 order of magnitude smaller than $K_r \omega^2$ and $\frac{K_m K_e}{R} \omega$ terms in Eq. (6).
- **Proportional Gain**
 K_p is the proportional gain of the control law, and it can be estimated by using the instantaneous angular acceleration while the rotor is changing from one trim condition to another. The formula used to estimate K_p is

$$J_r \dot{\omega} = \frac{K_m}{R} K_p e_\omega, \quad (20)$$

where $\dot{\omega}$ is the angular acceleration and e_ω is the difference angular speed between two trim conditions.

- **Integral Gain**
 K_i represents the integral gain of the control law and it can be estimated by observing the transition from one trim condition to another. Equations (6) and (10) can be applied to both trim conditions, thus the following equations can be obtained:

$$0 = -\frac{K_s}{J_r} - \frac{K_m K_e}{R J_r} \bar{\omega}_1 - \frac{K_r}{J_r} \bar{\omega}_1^2 + \frac{K_m K_i}{R J_r} \int e_{\omega 1} dt, \quad (21)$$

$$0 = -\frac{K_s}{J_r} - \frac{K_m K_e}{R J_r} \bar{\omega}_2 - \frac{K_r}{J_r} \bar{\omega}_2^2 + \frac{K_m K_i}{R J_r} \int e_{\omega 2} dt. \quad (22)$$

$\bar{\omega}_1$ and $\bar{\omega}_2$ are the steady-state angular speed for two trim conditions respectively, and both values are measurable. The difference between $\int(e_{\omega 1} dt)$ and $\int(e_{\omega 2} dt)$ can be obtained by integrating e_ω over transition interval between two consecutive trim conditions. Therefore, K_i can be estimated by subtracting Eq. (22) from Eq. (21).

Based on estimated initial values, parameter ranges are defined as shown in Table 5. For parameters calculated from datasheet, range is set as $\pm 10\%$ around initial values. For parameters calculated from experiment data, range is set as $\pm 50\%$ around initial values.

Table 5. Range of parameters.

Parameter	Initial value	Range
$R(\Omega)$	0.014	$\pm 10\%$
$J_r(\text{kg}\cdot\text{m}^2)$	3×10^{-5}	$\pm 50\%$
K_r	2.8×10^{-7}	$\pm 10\%$
K_m	0.01	$\pm 10\%$
K_e	0.012	$\pm 10\%$
K_s	10^{-2}	$\pm 50\%$
K_p	2.6×10^{-4}	$\pm 50\%$
K_i	7×10^{-2}	$\pm 50\%$

5.4. Result and comparison

The parameter identification is achieved by Matlab function “nlgreyest”, which estimates the unknown nonlinear grey-box model parameters based on the measured data. The function employs minimization schemes with embedded line searching methods for parameter estimation. The results are shown in Table 6.

Figures 17 and 18 show a comparison in the angular speed channel between identified semi-empirical model and

Table 6. Identified parameters.

Parameter	Value
$R(\Omega)$	0.0154
$J_r(\text{kg}\cdot\text{m}^2)$	4.5×10^{-5}
K_r	3.08×10^{-7}
K_m	0.009
K_e	0.0132
K_s	1.5×10^{-2}
K_p	1.3×10^{-4}
K_i	0.069

experimental data. The same data set is used for comparison since our early experiments show that data sets collected from multiple rotor tests are very consistent. We can observe that the model result matches the experiment data very well after the first five seconds since the initial value of integral gain K_i is estimated based on data of the transition interval between our interested trim condition and its consecutive trim conditions. Another factor is that, since most of the training data points are collected from the interested trim condition, this model is more effective for that trim condition.

In order to validate the model fidelity, Normalized Root Mean Square Error (NRMSE) is used as the fitness value in Matlab, as defined by

$$\text{fit}\% = 100\% \left(1 - \frac{\|p - \bar{p}\|}{\|p - \text{mean}(p)\|} \right), \quad (23)$$

where p is the validation data collected during experiment and \bar{p} is the output generated by the model. A total of 75.72% fitness shows that our model prediction fits well with the experimental data.

Another model validation standard is the Theil inequality coefficient [21] (TIC), which is defined by

$$\text{TIC} = \frac{\sqrt{\frac{1}{n} \sum_{i=1}^n (\bar{p} - p)^2}}{\sqrt{\frac{1}{n} \sum_{i=1}^n (\bar{p})^2 + \frac{1}{n} \sum_{i=1}^n (p)^2}}, \quad (24)$$

where n is the total sample amount, p is the validation data collected during experiment and \bar{p} is the output generated by ESC and BLDC model. TIC is a normalized value between [0, 1], and zero indicates a perfect matching. In practice, the threshold of TIC is commonly set at 0.25 according to [22]. As for TIC-based validation, results for Experiments 1 and 2 are 0.020 and 0.025, respectively. Both TIC values are much lower than the threshold value 0.25. Therefore, results

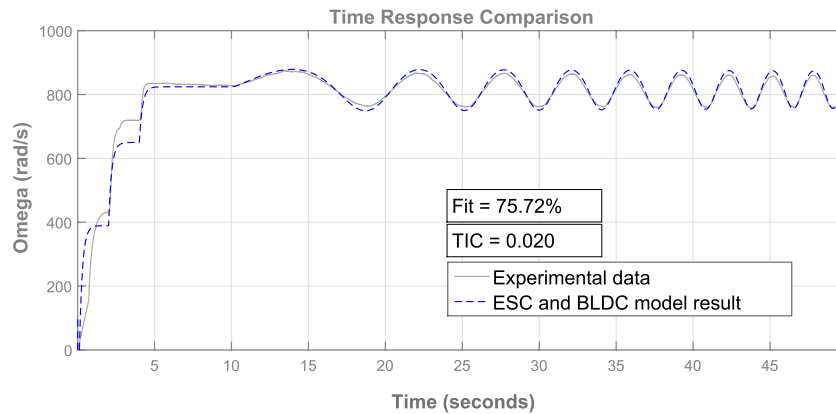


Fig. 17. Angular speed comparison between the semi-empirical MEP model prediction and experiment data (Experiment 1).

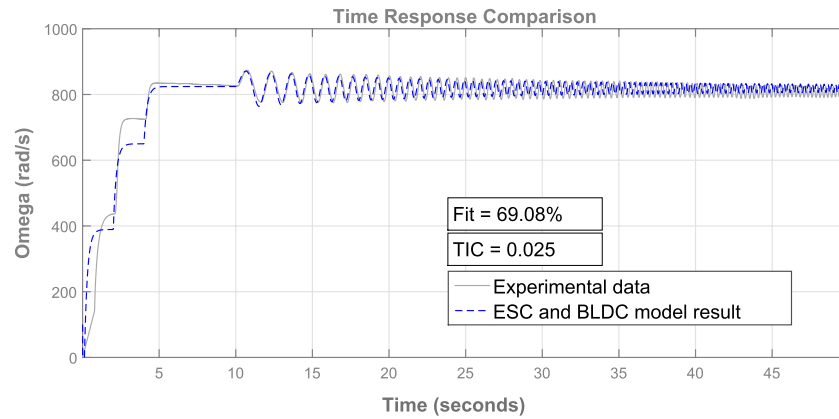


Fig. 18. Angular speed comparison between the semi-empirical MEP model prediction and experiment data (Experiment 2).

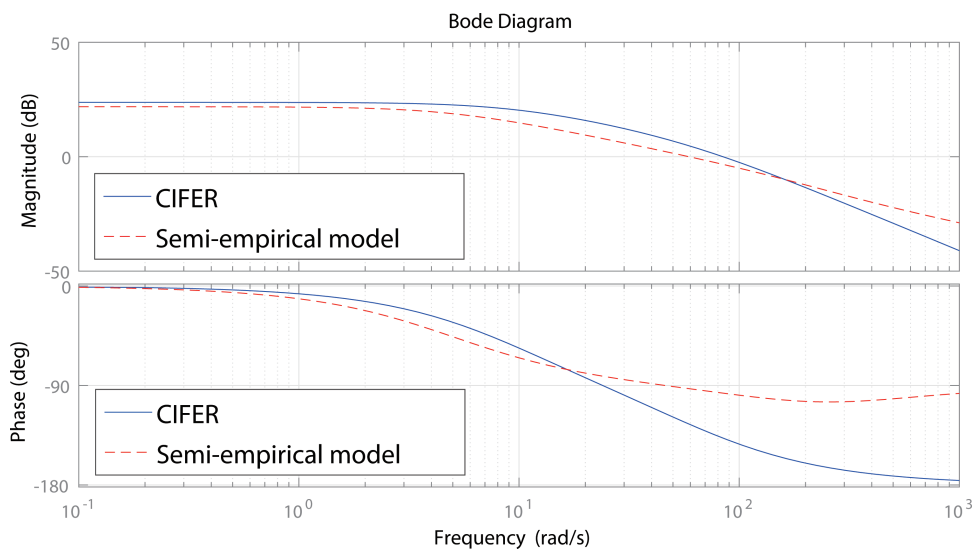


Fig. 19. Comparison of bode plots from CIFER and semi-empirical model for thrust channel.

indicate that identified ESC and BLDC model has sufficient accuracy.

After being linearized at the interested trim condition, the ESC and BLDC model is combined with propeller models, then compared with transfer function obtained through identification approach in Sec. 4. Input is throttle and output is thrust force. Bode plots for comparison are shown in Fig. 19.

The order of the system identified by CIFER is selected as second order for simplicity and the estimated bode plot shows that the second order model is able to achieve satisfactory accuracy for our application. The DC gain and bandwidth of CIFER identified system are 23.7 dB and 9.12 rad/s, respectively. The linearized semi-empirical MEP model aims to capture the low-order components (up to second-order) of rotor-driving dynamics at the interested

trim condition. Its DC gain and bandwidth are 21.8 dB and 4.95 rad/s, respectively.

The comparison shows that our semi-empirical MEP model can fit well with the CIFER identified model in the low frequency domain up to 10 rad/s, and the accuracy implies that our model is capable of predicting rotor-driving dynamics and can be integrated in real-time UAV dynamics and control applications.

6. Conclusions

To conclude, this paper presents a systematic modeling approach for rotor-driving dynamics including BLDC motor, ESC and propeller. Both steady state and frequency analyses

are conducted with sophisticated experiment setup. Transfer function models are estimated and proven to be reliable for up to 30 rad/s. A novel semi-empirical model is presented and validated by experimental data. The model is proven to fit well with frequency response results up to 10 rad/s and is promising in real-time implementation for UAV dynamics and control.

References

- [1] S. M. Ahmad, A. J. Chipperfield and M. O. Tokhi, Dynamic modelling and control of a 2-DOF twin rotor multi-input multi-output system, in *Proc. 26th IEEE Int. Conf. Ind. Electron., Control and Instrumentation (IECON 2000)*, (Nagoya, Japan, 2000), pp. 1451–1456.
- [2] B. Mettler, T. Kanade and M. B. Tischler, System identification modeling of a model-scale helicopter, tech. report CMU-RI-TR-00-03, Carnegie Mellon University, The Robotics Institute, Pittsburgh, PA (2000).
- [3] L. Ljung, Linear Model Identification, in *System identification toolbox: User's guide* (The MathWorks Inc., South Natick, MA, 1988).
- [4] B. M. Chen, T. H. Lee, K. Peng and V. Venkataramanan, *Hard Disk Drive Servo Systems*, 2nd edn. (Springer, New York, NY, 2006).
- [5] O. Moseler and R. Isermann, Application of model-based fault detection to a brushless DC motor, *IEEE Trans. Ind. Electron.* **47**(5) (2000) 1015–1020.
- [6] N. Matsui, Sensorless PM brushless DC motor drives, *IEEE Trans. Ind. Electron.* **42**(2) (1996) 300–308.
- [7] P. Pillay and R. Krishnan, Modeling, simulation, and analysis of permanent-magnet motor drives, Part II: The Brushless DC Motor Drive, *IEEE Trans. Ind. Electron.* **25**(2) (1989) 274–279.
- [8] P. Pillay and R. Krishnan, Modeling of permanent magnet motor drives, *IEEE Trans. Ind. Electron.* **35**(4) (1988) 537–541.
- [9] P. McKerrow, Modelling the Draganflyer four-rotor helicopter, in *IEEE Int. Conf. Robotics and Automation, 2004. ICRA '04. 2004*, (New Orleans, LA, 2004), Vol. 4, pp. 3596–3601.
- [10] P. Pounds, R. Mahony and J. Gresham, Towards Dynamically-Favourable Quad-Rotor Aerial Robots, in *Proc. 2004 Australasian Conf. Robotics & Automation*, (Canberra, Australia, 2004).
- [11] M. B. Tischler and R. K. Remple, *Aircraft and Rotorcraft System Identification* (AIAA Education, Reston, VA, 2006).
- [12] Universities Space Research Association (NAMS), *Comprehensive Identification from Frequency Responses Users Guide* (UCSC, Santa Cruz, CA, 2012).
- [13] G. Cai, B. M. Chen, K. Peng, M. Dong and T. H. Lee, Modeling and control of the yaw channel of a UAV helicopter, *IEEE Trans. Ind. Electron.* **55**(9) (2008) 3426–3434.
- [14] A. Hughes, Synchronous, Brushless D.C. and Switched Reluctance Drives, in *Electric Motors and Drives*, 3rd edn. (Newnes, Burlington, MA, 2006), pp. 340–365.
- [15] S. Bouabdallah, P. Murrieri and R. Siegwart, Design and control of an indoor micro quadrotor, in *Proc. ICRA '04. 2004 IEEE Int. Conf. Robotics and Automation, 2004*. (New Orleans, LA, 2004), pp. 4393–4398.
- [16] Y. Ke, An empirical model to rotor dynamics with brushless DC motor, Revised to 2016 (2016).
- [17] W. Johnson, Vertical Flight I, in *Helicopter Theory* (Dover Publications, New York, NY, 1994), pp. 45–55.
- [18] K. Li, A. Chen, K. Zhang and B. M. Chen, Improved efficiency electronic speed controller development for 3-phase brushless DC motor in unmanned aerial systems, in *Int. Micro Air Vehicle Competition and Conf.* (Beijing, P. R. China, 2016), pp. 167–172.
- [19] G. Cai, B. M. Chen and T. H. Lee, *Unmanned Rotorcraft Systems* (Springer Science & Business Media, New York, NY, 2011).
- [20] *General Motor Terminology* (The Motor & Motion Association, S. Dartmouth, MA, 2015).
- [21] M. B. Tischler and R. K. Remple, *Aircraft and Rotorcraft System Identification: Engineering Methods with Flight Test Examples* (American Institute of Aeronautics and Astronautics, Reston, VA, 2006).
- [22] G. Cai, T. Taha, J. Dias and L. Seneviratne, A framework of frequency-domain flight dynamics modeling for multi-rotor aerial vehicles, *J. Aerospace Eng.* **231**(1) (2017) 30–46.